ACS Catalysis

Research Article

pubs.acs.org/acscatalysis

Band Structure Engineering of Carbon Nitride: In Search of a Polymer Photocatalyst with High Photooxidation Property

Sheng Chu,[†,‡,§] Ying Wang,*[,†,‡,§] Yong Guo,[⊥] Jianyong Feng,[†] Cuicui Wang,[†,‡,§] Wenjun Luo,[†] Xiaoxing Fan,[†] and Zhigang Zou*[,†,‡,§]

[†]Eco-materials and Renewable Energy Research Center (ERERC), National Laboratory of Solid State Microstructures Nanjing University, Nanjing 210093, P. R. China.

[‡]School of Chemistry and Chemical Engineering, Nanjing University, Nanjing 210093, P. R. China

[§]Kunshan Innovation Institute of Nanjing University, Kunshan 215347, P. R. China

[⊥]School of Environment, Nanjing University, Nanjing 210093, P. R. China

Supporting Information

ABSTRACT: The electronic band structure of a semiconductor photocatalyst intrinsically controls its level of conduction band (CB) and valence band (VB) and, thus, influences its activity for different photocatalytic reactions. Here, we report a simple bottom-up strategy to rationally tune the band structure of graphitic carbon nitride (g-C_3N_4). By incorporating electron-deficient pyromellitic dianhydride (PMDA) monomer into the network of g-C_3N_4, the VB position can be largely decreased and, thus, gives a strong photooxidation capability. Consequently, the modified photocatalyst shows preferential activity for water oxidation over water reduction in comparison with g-C_3N_4. More strikingly, the active species involved in the photodegradation of methyl orange switches from photogenerated electrons to holes after band structure engineering. This work may provide guidance on designing efficient polymer photocatalysts with the desirable electronic structure for specific photoreactions.

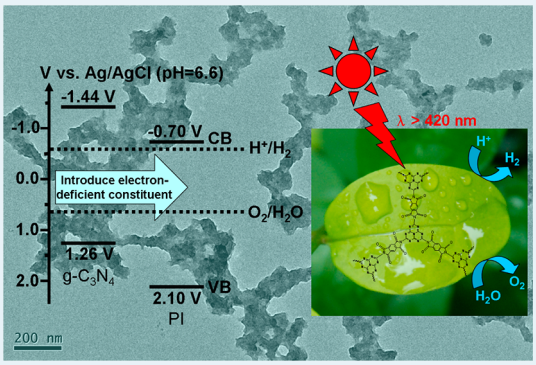

KEYWORDS: *polyimide, photocatalysis, band structure, water splitting, dye degradation*

1. INTRODUCTION

Semiconductor photocatalysis has attracted tremendous attention for its promising potential to settle intractable environmental and energy issues using abundant solar energy.[1,2] Splitting of water into hydrogen fuel and degradation of environmental pollutants are the two important aspects for photocatalytic applications. To date, the focus in this field lies in the development of novel efficient photocatalysts. For a practical large-scale application, an ideal photocatalyst would be inexpensive, sustainable, and stable and would work efficiently with visible light to utilize the main component of the solar spectrum. Within the photocatalyst family, TiO_2 is the most widely studied material because of its low cost, adequate stability, and suitable band edge positions with the redox potentials of water and various organic pollutants.[3] The bottom of the conduction band (CB) of TiO_2 is located at about −0.5 V vs NHE (pH = 7), which enables water reduction to form H_2, and the top of the valence band (VB) is at about 2.7 V, resulting in a high photooxidation capability for water oxidation and degradation of organic pollutants (Figure 1).[4] Unfortunately, the large bandgap (~3.2 ev) of TiO_2 limits its utilization of the solar spectrum only in the UV region. Doping TiO_2 with metal and nonmetal elements can create localized/delocalized states in the bandgap and, thus, extend its optical absorption in the visible region,[5,6] but doping is usually accompanied by accelerated photogenerated electron−hole recombination and reduced stability of the doped materials. Meanwhile, some noble metal complexes (e.g., Ru or Ir complex)[7] and rare-metal-based inorganic solids (e.g., Ga, Ge, or Ta (oxy)nitrides)[8] have been reported to be highly efficient photocatalysts under

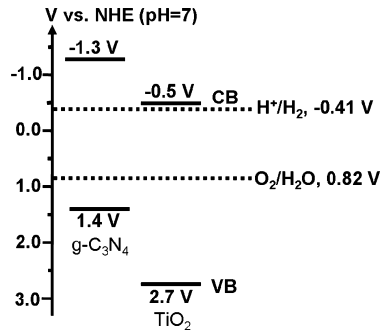

Figure 1. Schematic band structure of g-C_3N_4 and TiO_2.

Received: January 28, 2013
Revised: March 28, 2013
Published: March 29, 2013

visible light irradiation; however, scarcity and high cost are still issues for their large-scale applications.

Recently, it was reported that graphitic carbon nitride (g-C_3N_4) could function as a polymeric photocatalyst for hydrogen/oxygen evolution from water splitting in the presence of sacrificial reagents and degradation of organic pollutants under visible light irradiation.[9] In addition to its easy fabrication from the condensation of simple nitrogen-rich precursors (e.g., cyanamide or melamine), its low-cost and sustainable properties make g-C_3N_4 particularly attractive for solar-energy utilization. Moreover, the flexible structure of g-C_3N_4 allows plentiful organic schemes to tailor its chemical structure for the enhancement of its photocatalytic performance.[10] The bottom of the CB of g-C_3N_4 is located at about −1.3 V vs NHE (pH = 7) and is sufficient for water reduction to form hydrogen, whereas the top of the VB at about 1.4 V resulted in a small thermodynamic driving force for water and oxidationof organic pollutants (Figure 1).[4] Of the two half-reactions in water splitting, water oxidation is considered a more complicated process that involves four-electron transfer and reaction.[11] Accordingly, water oxidation to form oxygen represents a key half-reaction to ultimately achieve the goal of overall water splitting with a single chemical catalyst. In this regard, modulating the electronic band structure of g-C_3N_4 to decrease the VB position for the enhancement of photooxidation strength is highly desirable to improve the moderate performance of water oxidation and degradation of organic pollutants.

In this work, we present a facile bottom-up strategy to rationally tune the band structure of g-C_3N_4 toward enhanced photooxidation capability. By incorporating electron-deficient pyromellitic dianhydride (PMDA) constituent into the network of g-C_3N_4, the VB level can be lowered in a large range. Thus the modified photocatalyst features high photooxidation property for water oxidation and organic pollutants degradation.

2. EXPERIMENTAL SECTION

2.1. Sample Preparation Procedure. Melamine and PMDA were purchased from Shanghai Lingfeng Chemical Reagent Co., Ltd. and TCI Shanghai Chemical Reagent Co., Ltd., respectively. Polyimide (PI) was synthesized in the following procedure: Melem and PMDA with equal molar ratio (10 mmol, both 2.18 g) were mixed uniformly in an agate mortar. Then the mixture was put into a porcelain crucible covered loosely with a lid and heated at 7 °C/min up to 325 °C for 4 h. The resultant block solid was ground into powder and washed with water at 50 °C. Finally, the yellow product was filtered and dried to yield 3.52 g of PI. The mass yield was about 86%, which is ascribed to a small sublimation of PMDA monomer. Elemental analysis calculated for PI product $C_{13.36}H_{4.528}N_{10}O_{2.944}$: C, 45.56; H, 1.31; N, 39.77; O, 13.37%. Found: C, 41.15; H, 1.31; N, 40.13; O, 17.31%. Melem was synthesized by heating melamine at 425 °C for 4 h according to the literature.[12] Elemental analysis calculated for melem: H, 2.77; C, 33.03; N, 64.20. Found: H, 2.82; C, 32.83; N, 63.71. g-C_3N_4 was synthesized by heating 5 g of melamine at 550 °C for 4 h according to the literature.[13]

2.2. Characterization. Fourier transform infrared spectroscopy (FTIR) spectra were recorded on a Nicolet NEXUS870 spectrometer. Solid-state ^{13}C nuclear magnetic resonance (NMR) was performed on a Bruker Advance III 400 WB spectrometer equipped with a 9.4 T magnet. Elemental analysis was determined by an Elementar vario EL analyzer. X-ray diffraction (XRD) measurements were performed on a Rigaku Ultima III X-ray diffractometer using Cu Kα radiation. Thermogravimetric-differential scanning calorimetric (TG-DSC) analysis was performed on a Netzsch STA 449C in N_2 at a heating rate of 10 °C/min. The transmission electron microscope (TEM) image was recorded on a JEM-2100 electron microscope. The scanning electron microscope (SEM) image was obtained on a Hitachi S4800 FE-SEM system. UV−vis spectra were collected using a Shimadzu UV-2550 spectrometer. The specific surface area was measured using a Micromeritics Tristar-3000. The valence band X-ray photoelectron spectra (VBXPS) were undertaken using a PHI 5000 Versa Probe photoelectron spectrometer with monochromatized Al Kα X-ray radiation.

2.3. Photocatalytic Tests. A 300 W xenon lamp was used as the light source, and visible light irradiation was realized by attaching a 420 nm cutoff filter. For water splitting, the reactions were carried out in a closed gas-circulation system. The system was evacuated several times prior to irradiation. A H_2 evolving half-reaction was performed by dispersing 0.2 g catalyst in an aqueous solution (400 mL) containing methanol (10 vol %) as the scavenger and 1 wt % Pt as the cocatalyst. Pt was photodeposited on the catalyst by using H_2PtCl_6 dissolved in the reactant solution. The reactant solution was first irradiated under full arc light (λ > 300 nm) for 1 h to facilitate the deposition of Pt. For the O_2 evolving half-reaction, 0.2 g of catalyst was dispersed in an aqueous solution (400 mL) containing $AgNO_3$ (0.01 M) as the scavenger and La_2O_3 (0.4 g) as the pH buffer agent. The evolved H_2 and O_2 were analyzed by an online gas chromatograph (GC-14C, Shimadzu, TCD, Ar carrier).

For MO degradation, 0.2 g of catalyst was added to 100 mL MO solution (4 mg L^{-1}). Prior to irradiation, the solution was stirred in the dark for 1 h to reach the sorption equilibrium. During the irradiation, ∼4 mL of liquid was taken from the reaction cell at regular time intervals. The solution was analyzed by a UV−vis spectrometer (Shimadzu UV-1750). The concentration of MO was referred to the characteristic absorption at 464 nm. The N_2-purging experiment was conducted as follows: The reaction setup was vacuum-treated to remove O_2 and purged with high-purity N_2 (99.999%). Then the same process was repeated five times to eliminate O_2 completely. The N_2 gas was purged at a rate of 50 mL/min during the photodegradation process.

2.4. Electrochemical Analysis. The working electrode was prepared on fluoride tin oxide (FTO) glass substrates. First, 50 mg powder was mixed with 2 mL of acetone under sonication for 30 min to get a slurry. The slurry was then spread onto the FTO. After air-drying, the electrode was annealed at 300 °C for 30 min in air to improve the adhesion. The electrochemical properties were performed in a conventional three-electrode cell using an electrochemical analyzer (CHI-633C, Shanghai Chenhua, China). The working electrode was immersed in a sodium sulfate electrolyte solution (0.1 M), using a Pt sheet and a Ag/AgCl electrode as the counter and reference electrodes, respectively. The working electrode was irradiated from the back side (FTO substrate/semiconductor interface) to minimize the influence of the thickness of the semiconductor layer. The exposed area under illumination was 0.27 cm^2. For Mott−Schottky experiments, the perturbation signal was 10 mV with the frequency at 1 kHz. For electrochemical impedance spectroscopy (EIS) experiments, the perturbation

dx.doi.org/10.1021/cs4000624 | ACS Catal. 2013, 3, 912−919

signal was also 10 mV, but the frequency ranged from 200 kHz to 10 mHz.

2.5. Theoretical Calculations. All calculations were performed with the Gaussian 03 program. The B3LYP/6-31g method was used to optimize organic models. The highest occupied molecular orbital (HOMO) and lowest unoccupied molecular orbital (LUMO) were constructed with Gview program on the basis of the B3LYP/6-31g-optimized results.

3. RESULTS AND DISCUSSION

3.1. Synthesis and Structural Characterization. The desired polymer photocatalyst is synthesized via a bottom-up approach by copolymerizing melem (building units of g-C_3N_4) with PMDA at equal molar ratio, as shown in Scheme 1. The

Scheme 1. Reaction Scheme for the Synthesis of PI

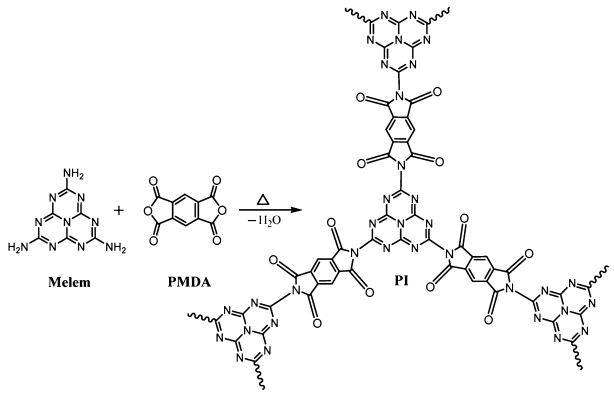

synthesis involves an imidization reaction with water released and gives a PI product. Analyzed from the framework of PI, it can be seen as a copolymer by uniformly incorporating PMDA constituent into the network of g-C_3N_4. We selected PMDA monomer to modify the band structure of g-C_3N_4 on the basis of two considerations: First, PMDA is a highly electron-deficient molecule due to the existence of two electron-withdrawing anhydride groups in the terminal and is thus expected to greatly influence the electronic structure of g-C_3N_4. Second, PMDA can be easily incorporated into the network of g-C_3N_4 because the formation of a five-membered imide ring is favorable from the point of thermodynamics.

The chemical structure of PI is verified by the combination of FTIR spectroscopy and solid-state ^{13}C NMR (Figure 2). In the FTIR spectrum, the characteristic absorption bands of polyimide are observed.[14] The three bands at 1774, 1725, and 722 cm^{-1} are assigned to the asymmetric stretching, the symmetric stretching, and the bending vibrations of imide carbonyl groups, respectively. The band at 1375 cm^{-1} is attributed to the stretching vibration of C−N−C in the five-membered imide ring. The sharp peak at around 805 cm^{-1} originates from heptazine ring units.[15] The several broad absorption bands between 1200 and 1600 cm^{-1} are contributed by aromatic carbon nitride heterocycles and benzene rings.[10b] In the ^{13}C NMR spectrum, the five signals can be ascribed to the five carbon positions of the presumed structure.[16,17] The signals of carbonyl carbons in the imide group and carbon atoms adjacent to the amino groups in heptazine are at 168 and 165 ppm, respectively. The high-field signal at 155 ppm belongs to the CN_3 groups in heptazine rings.[16] The two peaks in the region of 110−140 ppm can be assigned to aromatic carbons in benzene rings.[17]

The XRD patterns shown in Figure 3A also confirm the occurrence of an imidization reaction between melem and

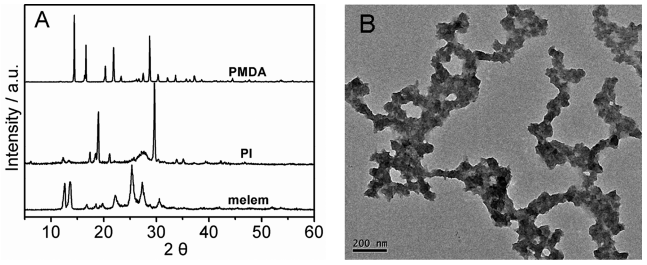

Figure 3. (A) XRD patterns of PI, PMDA and melem; (B) TEM image of PI.

PMDA. Several new sharp peaks in the range of 15−30° appear in th PI product, implying the formation of new species. No impurity phase belonging to the reactants is found in the PI product. The high crystallinity of PI indicates the high regularity of polymer chains, which is likely caused by the strong $\pi-\pi$ interactions between conjugated core units during the imidization reaction.[14b]

The TEM image shows that PI is composed of interconnected particles with sizes of ∼50 nm (Figure 3B), which can be identified as the cause of a highly cross-linking imidization reaction to form the product. SEM image of PI also displays a uniform and tight network-like structure (Figure S1, Supporting Information), but with three-dimensional field

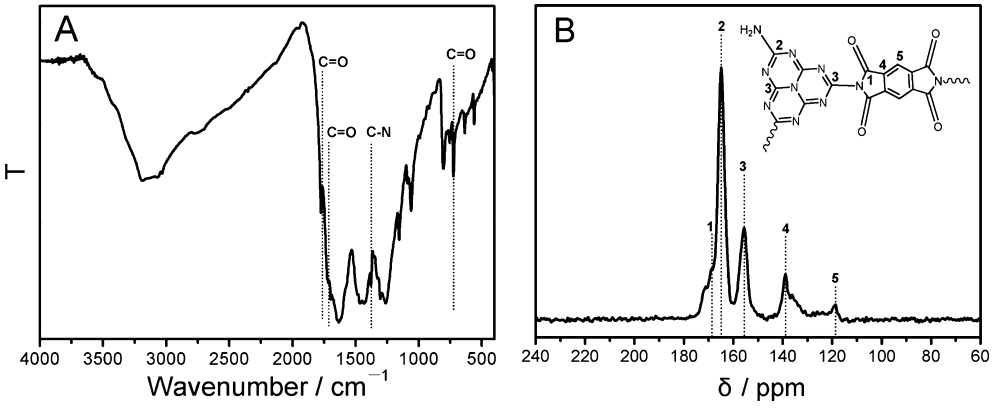

Figure 2. (A) FTIR and (B) ^{13}C NMR spectrum of PI.

dx.doi.org/10.1021/cs4000624 | ACS Catal. 2013, 3, 912−919

distribution due to the larger scene depth of SEM analysis compared with TEM observation. TG-DSC analysis shows a high thermal stability of PI with decomposition temperature at about 330 °C (Figure S2, Supporting Information). The endothermic peak around 400 °C is ascribed to the decomposition of PI.

3.2. Optical and Electronic Properties. The optical property of the PI sample is examined with UV−vis diffuse reflectance spectroscopy (Figure 4A). The yellow PI has the

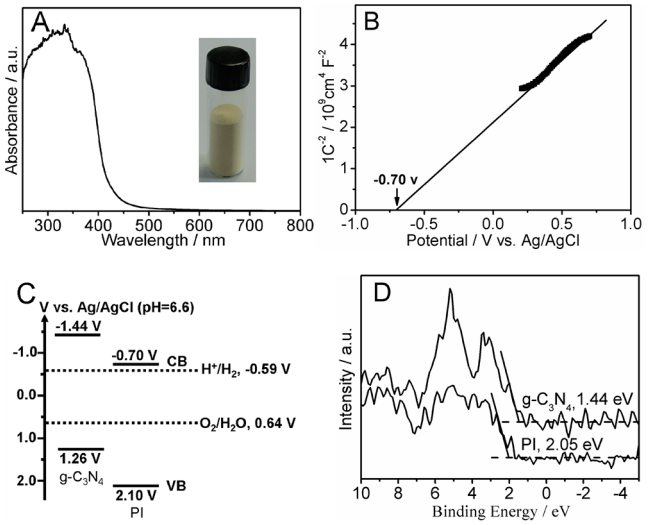

Figure 4. (A) UV−vis absorption spectrum and photograph (inset) of PI, (B) Mott−Schottky plot of PI, (C) band structure of g-C_3N_4 and PI, and (D) VB XPS of g-C_3N_4 and PI.

ability to absorb visible light. The absorption band edge of PI is determined to be 440 nm, corresponding to a bandgap energy of 2.8 eV, which is sufficiently large to overcome the energy criterion thermodynamically for the reaction involved in water-splitting (1.23 eV).

Aside from an appropriate bandgap, the matching of CB and VB levels of semiconductor photocatalyst with the redox potential of photocatalytic reaction is also important. To determine the relative positions of CB and VB edges, electrochemical Mott−Schottky experiment was performed (Figure 4B). The positive slope of the plot suggests that PI is an n-type semiconductor. From the intercept on the abscissa, the CB minimum is estimated to be −0.70 V vs Ag/AgCl at pH = 6.6. These data, combined with the bandgap energy, allow us to calculate the VB edge of PI at 2.10 V. Similarly, by using the above two experimental methods in combination (Figure S3, Supporting Information), the band structure of g-C_3N_4 can also be obtained (Figure 4C), which is consistent with the reported data.[10a] Compared with g-C_3N_4, the VB level of PI is much lowered, with a 0.84 V downshift from 1.26 to 2.10 V (Figure 4C). The trend of the VB edge downshift is also evidenced in the VBXPS of g-C_3N_4 and PI, although the observed downshift from 1.44 to 2.05 eV by 0.61 eV is a little smaller than 0.84 eV (Figure 4D). These results indicate that the incorporation of electron-withdrawing PMDA indeed greatly reduces the VB level of g-C_3N_4 and thus increases the photooxidation capability. Interestingly, after the band structure engineering, PI possesses a band structure similar to that of TiO_2, with a deep VB level of high photooxidation capability and an appropriate CB level that still enable water reduction. The minor difference is that the VB level of PI is ∼0.4 V higher than that of TiO_2, which is considerably important for the absorption of visible light that is incapable for TiO_2 without modification.

To gain better insight into the influence of PMDA introduction on electronic structure of g-C_3N_4, theoretical studies using density functional theory (DFT) calculations were also performed with cluster models. The incorporation of PMDA downshifts the energy level of HOMO from 1.80 to 2.61 eV, and the LUMO from −1.48 to −0.54 eV (Figure S4, Supporting Information). It is well-known that the HOMO and LUMO in a cluster are the counterparts of VB and CB levels in the material,[18] so the changing trends of energy levels obtained by theoretical studies are in good agreenment with the experimental results depicted in Figure 4C. This suggests that the proposed calculation method could provide good guidance for the rational band structure control of the organic semiconductor. More importantly, our results supply an effective route for the design of a polymer photocatalyst with enhanced photooxidation capability; that is, introduce an electron-withdrawing substituent into the polymer framework to decrease the VB level. Interestingly, a similar strategy for the electronic structure optimization is also used in the field of organic solar cells to achieve better efficiency.[19] For example, Zhou et al. found that the introduction of electron-withdrawing fluorine atoms into a conjugated polymer reduces both the HOMO and LUMO energy levels, thus creating a high-performance polymer solar cell.[19b]

For an optimal photocatalyst, it not only needs suitable band edge positions and an appropriate bandgap to absorb enough light for the generation of charge carriers (electron−hole pairs) but also requires the ability to efficiently transfer and separate the carriers. On the basis of DFT calculations, the HOMO of g-C_3N_4 derives exclusively from the combination of heterocyclic nitrogen p_z orbitals, and LUMO mainly consists of C−N bond orbitals (Figure S5, Supporting Information), which is in agreement with a previous report.[20] After coupling with PMDA, the HOMO is not much changed and still locates on the melem moiety, whereas the LUMO shifts from the melem to the PMDA moiety (Figure 5A, B). This is in reasonable agreement with the assumption that PMDA has a strong electron-withdrawing ability. On the other hand, the preferred active sites of PI for oxidation reactions are located at the melem and, for reduction reactions, are at the PMDA. Therefore, the incorporation of electron-withdrawing PMDA helps not only to modify the electronic band structure but also to separate the reduction and oxidation sites, which benefits the spatial charge separation and, thus, the photocatalytic process.[21,22]

Electrostatic potential (ESP) distribution can also provide useful information to analyze the reactive sites.[23] The negative and positive parts are expected to be the favorable sites for the reduction and oxidation reaction, respectively. Thus, we investigate the distribution of ESP on the g-C_3N_4 and PI surfaces through DFT calculations, as shown in Figures S6 (Supporting Information) and 5C. The most negative and positive potentials are assigned to be red and blue, respectively. According to Figure S6 (Supporting Information), the negative potentials of g-C_3N_4 locate mainly at triangular edge nitrogen atoms in melem units, whereas the positive potentials are at the other parts of melem. After incorporating an electron-withdrawing PMDA constituent, there is an obvious change in the negative potentials: the dominating negative parts shift from the nitrogen atoms of the melem to the oxygen atoms of the PMDA moiety. This is not unexpected, considering that

dx.doi.org/10.1021/cs4000624 | ACS Catal. 2013, 3, 912−919

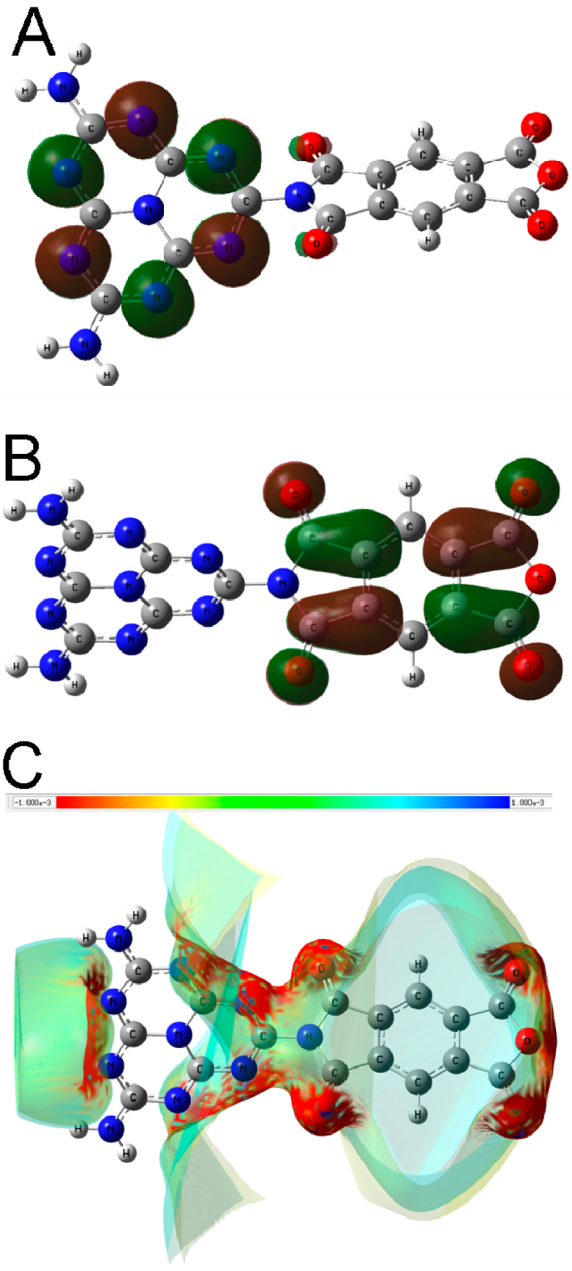

Figure 5. DFT calculated HOMO (A), LUMO (B) and ESP distribution (C) of optimized PI model.

oxygen has a larger electronegativity than nitrogen (3.44 vs 3.04). So it is deduced that the reduction sites have a large shift from melem to PMDA, which agrees well with the calculated change of the LUMO position and also implies the redox sites are separated after the incorporation of PMDA into g-C_3N_4.

3.3. Photocatalytic Activities. The photocatalytic activities of g-C_3N_4 and PI for the two half-reactions of water splitting are examined. A H_2-evolving half-reaction is tested first with methanol as a sacrificial electron donor and Pt (1 wt %) as a cocatalyst under visible light irradiation ($\lambda > 420$ nm). The Pt particles are well-dispersed on PI, and the average particle size is ~2−3 nm (Figure S7, Supporting Information). As shown in Figure 6A, the H_2 evolution rate of PI (20.6 μmol h^{-1}) is about 3 times as high as that of g-C_3N_4 (7.0 μmol h^{-1}), despite its weaker reducing power of photoinduced electrons compared with that of g-C_3N_4. Further considering the similar optical absorption, particle size (TEM image of g-C_3N_4 is shown in Figure S8, Supporting Information) and surface area of PI and g-C_3N_4 (8 and 10 m^2 g^{-1}, respectively), we reason that the improved activity is ascribed to the enhanced charge transfer and separation, since the incorporation of PMDA into g-C_3N_4 helps to redistribute electronic potential and separate redox sites.

To gain more information about the properties of charge carriers, photocurrent measurement and an EIS experiment were performed (Figure 6B). The photocurrent output of PI is much higher than that of g-C_3N_4 over different bias potentials under visible light irradiation, indicating a more efficient transfer and separation of photogenerated charge carriers.[24] The charge separation efficiency was also investigated by EIS analysis, with the arc radius reflecting the reaction rate occurring at the surface of the electrode.[25] The smaller arc radius of PI over g-C_3N_4 indicates its higher separation efficiency of photogenerated charge carriers.

We then tested the O_2 evolving half-reaction, with $AgNO_3$ as a sacrificial agent under visible light irradiation. In the presence of $AgNO_3$ as electron acceptor, the photogenerated electrons can be easily consumed via the reduction of Ag^+ to form Ag, so the efficiency of water oxidation to form O_2 is largely determined by the oxidative power of the photogenerated holes.[26] As shown in Figure 7, the initial O_2 evolution rate of the PI is estimated to be 7.7 μmol h^{-1}, which is about an order of magnitude larger than that of g-C_3N_4 (0.8 μmol h^{-1}). Compared with the 3-fold increase in the H_2 evolution rate after incorporating PMDA into g-C_3N_4, intriguingly, the increasing ratio of the O_2 evolution rate is more pronounced. This photoreaction preference is in good agreement with the downward-shift VB position after band structure engineering. It is considered that in addition to the improved charge transfer and separation, the much enhanced photooxidative capability of PI over g-C_3N_4 also contributes to the increase in the O_2 evolution rate. Compared with g-C_3N_4, PI has a greatly lowered VB level (by 0.8 V), giving a much higher thermodynamic driving force for water oxidation and, consequently, the O_2 evolving activity. A similar phenomenon is also found with sulfur-mediated g-C_3N_4. Owing to the larger electronegativity of sulfur than carbon (2.58 vs 2.55), doping g-C_3N_4 with sulfur at the carbon site leads to a downshift of the VB level by ~0.2 V and, thus, promotes the O_2 evolution rate.[27] Both of these results verify the positive effects of lowering the VB position to enhance the O_2 evolving activity. From Figure 7, we note that the O_2 evolution rates of PI and g-C_3N_4 decrease gradually with the reaction time as a result of the surface of the photocatalyst being covered with reduced black Ag particles that hinder light absorption and obstruct active sites.[28]

Wavelength dependence of the rates of H_2 and O_2 evolution for PI was examined using different band-pass filters (Figure 8). Both the H_2 and O_2 evolution rates match well with the optical absorption spectrum of PI, indicating the two half-reactions are really driven by the bandgap transition of PI. According to the amount of evolved gases and light intensity, the apparent quantum yields (AQY) at different incident wavelengths can be calculated.[8b] The AQY of PI for H_2 and O_2 at 420 nm (half-width, 14 nm) with a light intensity of 3×10^{21} photons/h is estimated to be 0.3% and 0.2%, respectively.

To further demonstrate the strong photooxidative capability of PI, an organic dye degradation experiment using methyl orange (MO) as a model pollutant was performed. Figure 9

dx.doi.org/10.1021/cs4000624 | ACS Catal. 2013, 3, 912−919

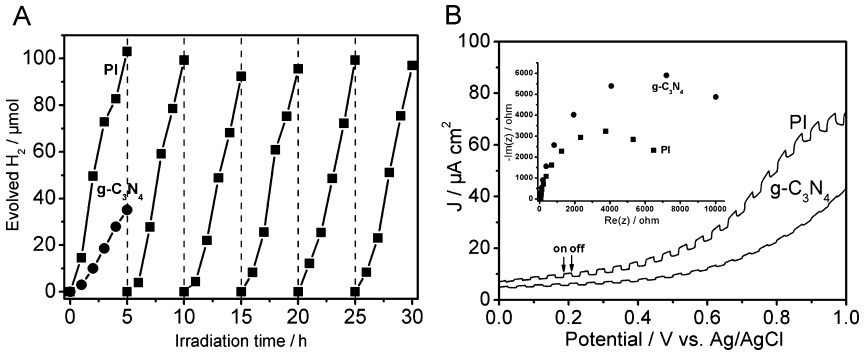

Figure 6. (A) Time course of H_2 evolution from a 10 vol % aqueous methanol solution by Pt-deposited PI and g-C_3N_4 under visible light irradiation (λ > 420 nm); (B) Photocurrent–potential curves of PI and g-C_3N_4 electrode in 0.1 M Na_2SO_4 aqueous solution under visible light irradiation. The inset is EIS Nyquist plots of PI and g-C_3N_4 in the dark.

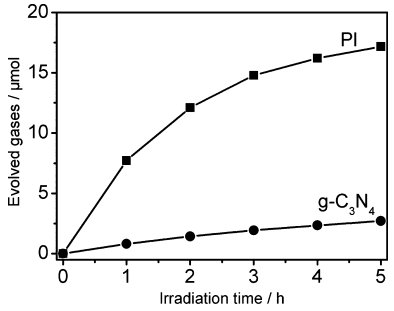

Figure 7. Time course of O_2 evolution from a 0.01 M aqueous $AgNO_3$ solution by bare PI and g-C_3N_4 under visible light irradiation (λ > 420 nm).

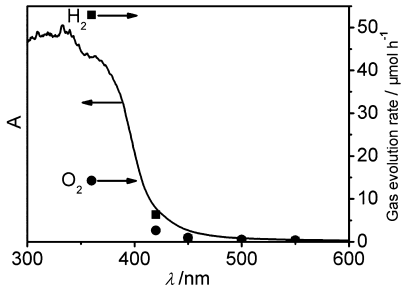

Figure 8. Wavelength dependence of H_2 and O_2 evolution rates over Pt-deposited PI and bare PI, respectively. The H_2 and O_2 rates are determined by the first 2 and 1 h, respectively.

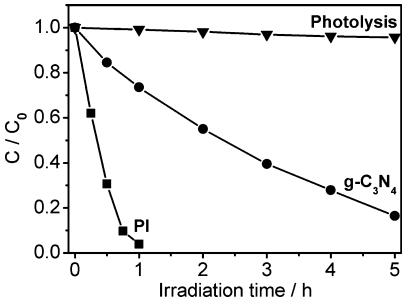

Figure 9. Time courses of MO degradation by PI and g-C_3N_4 under visible light irradiation (λ > 420 nm).

shows the degradation of MO over g-C_3N_4 and PI under visible light irradiation as a function of the illumination time. MO photolysis (without photocatalyst) is negligible because of the stable structure of MO under light irradiation.[29] In comparation with g-C_3N_4, PI exhibits superior photodegradation activity, with MO degraded completely after 1 h of light irradiation. For a better comparison of the photocatalytic efficiency of g-C_3N_4 and PI, kinetic analysis for the photodegradation of MO was also investigated (Figure S9, Supporting Information). It shows that the two degradation processes follow a pseudo-first-order reaction. The degradation rate of MO over PI is estimated to be 3.34 h^{-1}, which is about an order of magnitude higher than that of g-C_3N_4 (0.35 h^{-1}). The stronger oxidative power of photogenerated holes of PI over g-C_3N_4 is identified as the main cause of the improvement.

To confirm this, control experiments by adding KI as a hole scavenger in the photodegradation system were conducted (Figure 10).[30] It was observed that the photodegrading rate of

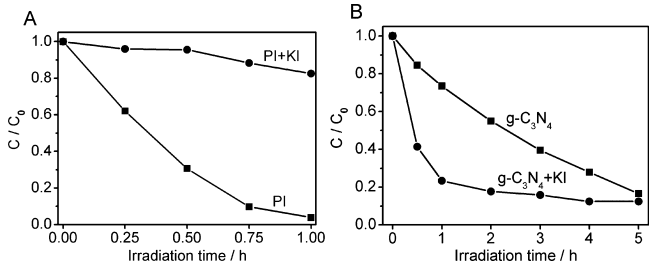

Figure 10. Effects of KI as hole scavenger on the degradation of MO in the presence of PI (A) and g-C_3N_4 (B) under visible light irradiation (λ > 420 nm).

MO over PI decreases significantly after the addition of KI, indicating the photogenerated holes play a crucial role in the case of PI. With g-C_3N_4, in contrast, the photodegrading activity does not decrease, but increases, after the introduction of KI. (The increase in activity can be explained as follows: The photocatalytic process involves simultaneous reactions of photogenerated electrons and holes. Because of the moderate photooxidation capability of g-C_3N_4, it is considered that the slow consumption of photogenerated holes in VB is the rate-limiting step in MO degradation. After adding KI as a hole scavenger, the kinetic bottleneck is much alleviated, since the oxidation of I^- to I_2 is favorable from the point of dynamics.[31]) This implies that photogenerated holes are not the active species for MO degradation over g-C_3N_4.

A further investigation was to determine the effect of photogenerated electrons on MO degradation over PI and g-C_3N_4. Generally, the photogenerated electron works via the reduction of O_2 to form reactive oxygen species, such as the

dx.doi.org/10.1021/cs4000624 | ACS Catal. 2013, 3, 912–919

superoxide radical anion ($O_2^{\bullet-}$) and hydroxyl radical (OH•).[32] Therefore, N_2-purging experiments to exclude O_2 were conducted (Figure 11). It was found that MO can be completely degraded by PI within 1 h of light irradiation, but no degradation occurs at all with g-C_3N_4, even after 5 h. This result indicates that the O_2 reduction process initiated by photogenerated electrons is the cause of the MO degradation over g-C_3N_4, which is not the case for PI.

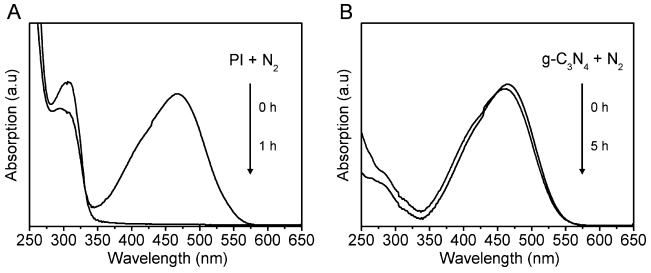

Figure 11. UV−vis spectroscopic changes of MO in an N_2-purged system in the presence of PI (A) and g-C_3N_4 (B) under visible light irradiation (λ > 420 nm).

It is interesting to note that the photoreaction pathways are switched after the band structure engineering. The active species for MO degradation over g-C_3N_4 and PI are attributed to photogenerated electrons and holes, respectively. The stronger photooxidative capability of PI over g-C_3N_4 enables photogenerated holes to have a large thermodynamic driving force to directly involve in MO degradation and act as the dominating active species. Our result suggests the possibility of tuning the photoreaction pathways by rationally engineering the band structure of the polymer photocatalyst.

4. CONCLUSIONS

We report a simple bottom-up strategy by incorporating electron-deficient PMDA monomer to tune the band structure of g-C_3N_4 toward enhanced photooxidation capability. The modified photocatalyst features preferential activity for water oxidation over water reduction compared with g-C_3N_4. Moreover, the active species involved in the photodegradation of MO switches from photogenerated electrons to holes after band structure engineering. This work may shed light on a general approach for designing polymer photocatalysts with desired band structures for targeted photoreactions.

■ ASSOCIATED CONTENT

Supporting Information

SEM image of PI; optical and electronic properties of g-C_3N_4; DFT calculations of PI and g-C_3N_4; kinetic analysis of MO photodegradation. This information is available free of charge via the Internet at http://pubs.acs.org/.

■ AUTHOR INFORMATION

Corresponding Author

*E-mail: wangy@nju.edu.cn.

Notes

The authors declare no competing financial interest.

■ ACKNOWLEDGMENTS

This work was financially supported by NSFC (21273111 and 21273106). The authors thank the Analysis Center and High Performance Computing Center of Nanjing University for the sample characterization and theoretical calculations, respectively.

■ REFERENCES

(1) Hoffmann, M. R.; Martin, S. T.; Choi, W.; Bahnemann, D. W. *Chem. Rev.* **1995**, *95*, 69.
(2) Chen, X. B.; Shen, S. H.; Guo, L. J.; Mao, S. S. *Chem. Rev.* **2010**, *110*, 6503.
(3) (a) Chen, X. B.; Mao, S. S. *Chem. Rev.* **2007**, *107*, 2891. (b) Liu, G.; Wang, L. Z.; Yang, H. G.; Cheng, H. M.; Lu, G. Q. *J. Mater. Chem.* **2010**, *20*, 831. (c) Kubacka, A.; Fernandez-Garcia, M.; Colon, G. *Chem. Rev.* **2012**, *112*, 1555.
(4) Cui, Y. J.; Ding, Z. X.; Liu, P.; Antonietti, M.; Fu, X. Z.; Wang, X. C. *Phys. Chem. Chem. Phys.* **2012**, *14*, 1455.
(5) (a) Choi, W.; Termin, A.; Hoffmann, M. R. *J. Phys. Chem.* **1994**, *98*, 13669. (b) Yu, J. C.; Li, G. S.; Wang, X. C.; Hu, X. L.; Leung, C. W.; Zhang, Z. D. *Chem. Commun.* **2006**, 2717.
(6) (a) Asahi, R.; Morikawa, T.; Ohwaki, T.; Aoki, K.; Taga, Y. *Science* **2001**, *293*, 269. (b) Zhao, W.; Ma, W. H.; Chen, C. C.; Zhao, J. C.; Shuai, Z. G. *J. Am. Chem. Soc.* **2004**, *126*, 4782. (c) Liu, G.; Zhao, Y.; Sun, C.; Li, F.; Lu, G. Q.; Cheng, H. M. *Angew. Chem., Int. Ed.* **2008**, *47*, 4516.
(7) (a) Esswein, A. J.; Nocera, D. G. *Chem. Rev.* **2007**, *107*, 4022. (b) Chen, W.; Rein, F. N.; Rocha, R. C. *Angew. Chem., Int. Ed.* **2009**, *48*, 9672.
(8) (a) Maeda, K.; Domen, K. *J. Phys. Chem. C* **2007**, *111*, 7851. (b) Kudo, A.; Miseki, Y. *Chem. Soc. Rev.* **2009**, *38*, 253.
(9) (a) Wang, X. C.; Maeda, K.; Thomas, A.; Takanabe, K.; Xin, G.; Carlsson, J. M.; Domen, K.; Antonietti, M. *Nat. Mater.* **2009**, *8*, 76. (b) Maeda, K.; Wang, X. C.; Nishihara, Y.; Lu, D. L.; Antonietti, M.; Domen, K. *J. Phys. Chem. C* **2009**, *113*, 4940. (c) Yan, S. C.; Li, Z. S.; Zou, Z. G. *Langmuir* **2009**, *25*, 10397.
(10) (a) Zhang, J. S.; Chen, X. F.; Takanabe, K.; Maeda, K.; Domen, K.; Epping, J. D.; Fu, X. Z.; Antonietti, M.; Wang, X. C. *Angew. Chem., Int. Ed.* **2010**, *49*, 441. (b) Zhang, J. S.; Zhang, G. G.; Chen, X. F.; Lin, S.; Mohlmann, L.; Dolega, G.; Lipner, G.; Antonietti, M.; Blechert, S.; Wang, X. C. *Angew. Chem., Int. Ed.* **2012**, *51*, 3183.
(11) (a) Kanan, M. W.; Nocera, D. G. *Science* **2008**, *321*, 1072. (b) Sala, X.; Romero, I.; Rodríguez, M.; Escriche, L.; Llobet, A. *Angew. Chem., Int. Ed.* **2009**, *48*, 2842. (c) Yi, Z. G.; Ye, J. H.; Kako, N, T.; Ouyang, S. X.; Stuart-Williams, H.; Yang, H.; Cao, J. Y.; Luo, W. J.; Li, Z. S.; Liu, Y.; Withers, R. L. *Nat. Mater.* **2010**, *9*, 559. (d) Duan, L. L.; Bozoglian, F.; Mandal, S.; Stewart, B.; Privalov, T.; Llobet, A.; Sun, L. C. *Nat. Chem.* **2012**, *4*, 418.
(12) (a) Sattler, A.; Schönberger, S.; Schnick, W. *Z. Anorg. Allg. Chem.* **2010**, *636*, 476. (b) Makowski, S. J.; Köstler, P.; Schnick, W. *Chem.—Eur. J.* **2012**, *18*, 3248.
(13) Hong, J. D.; Xia, X. Y.; Wang, Y. S.; Xu, R. *J. Mater. Chem.* **2012**, *22*, 15006.
(14) (a) Zeng, S. Z.; Guo, L. M.; Cui, F. M.; Gao, Z.; Zhou, J.; Shi, J. L. *Macromol. Chem. Phys.* **2010**, *211*, 698. (b) Chu, S.; Wang, Y.; Guo, Y.; Zhou, P.; Yu, H.; Luo, L. L.; Kong, F.; Zou, Z. G. *J. Mater. Chem.* **2012**, *22*, 15519.
(15) Niu, P.; Zhang, L. L.; Liu, G.; Cheng, H. M. *Adv. Funct. Mater.* **2012**, *22*, 4763.
(16) (a) Jurgens, B.; Irran, E.; Senker, J.; Kroll, P.; Muller, H.; Schnick, W. *J. Am. Chem. Soc.* **2003**, *125*, 10288. (b) Lotsch, B. V.; Sehnert, M. J.; Seyfarth, L.; Senker, J.; Oeckler, O.; Schnick, W. *Chem.—Eur. J.* **2007**, *13*, 4969.
(17) (a) Singh, D.; Narula, A. K. *J. Therm. Anal. Calorim.* **2010**, *100*, 199. (b) Ren, S. J.; Dawson, R.; Laybourn, A.; Jiang, J. X.; Khimyak, Y.; Adams, D. J.; Cooper, A. I. *Polym. Chem* **2012**, *3*, 928.
(18) Guo, Y.; Kong, F.; Chu, S.; Luo, L. L.; Yang, J. C.; Wang, Y.; Zou, Z. G. *RSC Adv.* **2012**, *2*, 5585.
(19) (a) Roncali, J. *Macromol. Rapid Commun.* **2007**, *28*, 1761. (b) Price, S. C.; Stuart, A. C.; Yang, L. Q.; Zhou, H. X.; You, W. *J. Am. Chem. Soc.* **2011**, *133*, 4625. (c) Mishra, A.; Bauerle, P. *Angew. Chem., Int. Ed.* **2012**, *51*, 2020.

(20) Ma, X. G.; Lv, Y. H.; Xu, J.; Liu, Y. F.; Zhang, R. Q.; Zhu, Y. F. *J. Phys. Chem. C* **2012**, *116*, 23485.
(21) (a) Guo, Y.; Chu, S.; Yan, S. C.; Wang, Y.; Zou, Z. G. *Chem.Commun.* **2010**, *46*, 7325. (b) Marchanka, A.; Maier, S. K.; Hoger, S.; Gastel, M. V. *J. Phys. Chem. B* **2011**, *115*, 13526.
(22) (a) Maeda, K.; Xiong, A.; Yoshinaga, T.; Ikeda, T.; Sakamoto, N.; Hisatomi, T.; Takashima, M.; Lu, D. L.; Kanehara, M.; Setoyama, T.; Teranishi, T.; Domen, K. *Angew. Chem., Int. Ed.* **2010**, *49*, 4096. (b) Lin, F.; Wang, D. E.; Jiang, Z. X.; Ma, Y.; Li, J.; Li, R. G.; Li, C. *Energy. Environ. Sci.* **2012**, *5*, 6400.
(23) (a) Zhang, G. L.; Zhang, H.; Li, D. P.; Chen, D.; Yu, X. Y.; Liu, B.; Li, Z. S. *Theor. Chem. Acc.* **2008**, *121*, 109. (b) Chi, X. L.; Li, D. W.; Zhang, H. Q.; Chen, Y. S.; Garcia, V.; Garcia, C.; Siegrist, T. *Org. Electron.* **2008**, *9*, 234.
(24) Zhang, Y. J.; Antonietti, M. *Chem.—Asian J.* **2010**, *5*, 1307.
(25) Wang, Y. J.; Bai, X. J.; Pan, C. S.; He, J.; Zhu, Y. F. *J. Mater. Chem.* **2012**, *22*, 11568.
(26) Liu, G.; Pan, J.; Yin, L. C.; Irvine, J. T. S.; Li, F.; Tan, J.; Wormald, P.; Cheng, H. M. *Adv. Funct. Mater.* **2012**, *22*, 3233.
(27) Zhang, J. S.; Sun, J. H.; Maeda, K.; Domen, K.; Liu, P.; Antonietti, M.; Fu, X. Z.; Wang, X. C. *Energy Environ. Sci.* **2011**, *4*, 675.
(28) (a) Ishikawa, A.; Takata, T.; Kondo, J. N.; Hara, M.; Kobayashi, H.; Domen, K. *J. Am. Chem. Soc.* **2002**, *124*, 13547. (b) Hisatomi, T.; Hasegawa, K.; Teramura, K.; Takata, T.; Hara, M.; Domen, K. *Chem. Lett.* **2007**, *36*, 558.
(29) Gao, F.; Chen, X. Y.; Yin, K. B.; Dong, S.; Ren, Z. F.; Yuan, F.; Yu, T.; Zou, Z. G.; Liu, J. M. *Adv. Mater.* **2007**, *19*, 2889.
(30) Kou, J. H.; Li, Z. S.; Yuan, Y. P.; Zhang, H. T.; Wang, Y.; Zou, Z. G. *Environ. Sci. Technol.* **2009**, *43*, 2919.
(31) Lanzarini, E.; Antognazza, M. R.; Biso, M.; Ansaldo, A.; Laudato, L.; Bruno, P.; Metrangolo, P.; Resnati, G.; Ricci, D.; Lanzani, G. *J. Phys. Chem. C* **2012**, *116*, 10944.
(32) (a) Palominos, R.; Freer, J.; Mondaca, M. A.; Mansilla, H. D. *J. Photochem. Photobiol. A* **2008**, *193*, 139. (b) Yan, S. C.; Li, Z. S.; Zou, Z. G. *Langmuir* **2010**, *26*, 3894.